Chemosphere 237 (2019) 124478

Contents lists available at ScienceDirect

Chemosphere

journal homepage: www.elsevier.com/locate/chemosphere

Enhanced activation of peroxymonosulfte by $LaFeO_3$ perovskite supported on Al_2O_3 for degradation of organic pollutants

Shaohua Wu [a, b], Yan Lin [a, b], Chunping Yang [a, b, c, *], Cheng Du [a, c], Qing Teng [a, c, **], Yin Ma [a, c], Dongmei Zhang [a, c], Lijun Nie [a, c], Yuanyuan Zhong [a, c]

[a] School of Environmental Science and Engineering, Guangdong University of Petrochemical Technology, Maoming, Guangdong, 525000, China
[b] College of Environmental Science and Engineering, Hunan University and Key Laboratory of Environmental Biology and Pollution Control (Hunan University), Ministry of Education, Changsha, Hunan, 410082, China
[c] Guangdong Provincial Key Laboratory of Petrochemical Pollution Processes and Control, Guangdong University of Petrochemical Technology, Maoming, Guangdong, 525000, China

HIGHLIGHTS

- Catalysts of $LaFeO_3$ perovskites were successfully prepared by the citric sol-gel method.
- Support effect on catalytic properties of $LaFeO_3$ for PMS activation was reported.
- $LaFeO_3/Al_2O_3$ showed the highest activity for AO7 degradation than other supported catalysts.
- Surface-bound sulfate radical was identified responsible for AO7 degradation.

GRAPHICAL ABSTRACT

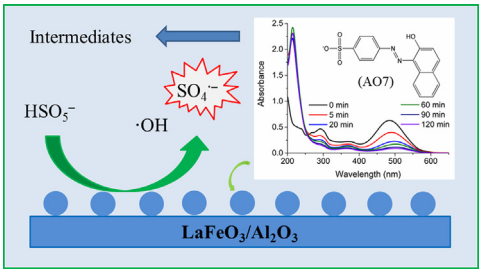

ARTICLE INFO

Article history:
Received 6 May 2019
Received in revised form
6 July 2019
Accepted 28 July 2019
Available online 29 July 2019

Handling Editor: Jun Huang

Keywords:
Support
Perovskite
Peroxymonosulfate
Degradation kinetic
Sulfate radical

ABSTRACT

In this study, the effect of various supports on activation of peroxymonosulfate and consequent degradation of Acid Orange 7 (AO7) in aqueous solutions was examined at the presence of $LaFeO_3$ perovskite as catalyst. Results showed that the AO7 degradation efficiency by $LaFeO_3$ supported on different supports was in an order of $LaFeO_3/Al_2O_3$ (86.2%) > $LaFeO_3$ (70.8%) > $LaFeO_3/CeO_2$ (59.0%) > $LaFeO_3/SiO_2$ (52.3%) > $LaFeO_3/TiO_2$ (32.2%). Moreover, the pseudo first-order rate constant for AO7 degradation by $LaFeO_3/Al_2O_3$ was 3.2 times than that by $LaFeO_3$. The enhancement was attributed to its large surface area, abundant chemisorbed surface-active oxygen, redox property and faster electron transfer. AO7 degradation and the leaching of iron ions decreased with the increase of pH. Data of electron spin resonance spectroscopy and quenching experiments revealed that sulfate and hydroxyl radicals were generated on $LaFeO_3/Al_2O_3$ surface, while sulfate radicals were identified to be the main reactive species responsible for AO7 degradation. Mechanisms for peroxymonosulfate activation were consequently proposed. Furthermore, $LaFeO_3/Al_2O_3$ catalyst exhibited a superior stability after five cycles. This work provides a new approach for design of iron-based perovskite catalysts with high and stable catalytic activity for removal of organic pollutants from aqueous solutions.

* Corresponding author. School of Environmental Science & Engineering, Guangdong University of Petrochemical Technology, Maoming, Guangdong, 525000, China.
** Corresponding author. School of Environmental Science & Engineering, Guangdong University of Petrochemical Technology, Maoming, Guangdong, 525000, China.
E-mail addresses: yangc@hnu.edu.cn (C. Yang), tengqing@gdupt.edu.cn (Q. Teng).

https://doi.org/10.1016/j.chemosphere.2019.124478
0045-6535/

1. Introduction

Peroxymonosulfate (PMS) based-advanced oxidation processes have drawn much interest for degradation of recalcitrant contaminants from water in the last decades (Wang and Wang, 2018; Wu et al., 2018b; Yang et al., 2018). Generally, PMS can be activated by base (Qi et al., 2016), heat (Ji et al., 2015), UV (Xu et al., 2017), metal-free carbon (Long et al., 2019; Zeng et al., 2018) and transition metals (Zhao et al., 2019) to generate sulfate radicals ($SO_4^{\bullet-}$). Among, cobalt was considered as the most efficient PMS activator (Hu and Long, 2016), while the adverse effect of leached cobalt ion confined its practical application. Consequently, the development of green efficient heterogeneous catalysts for PMS activation has become a priority.

Recent studies have demonstrated that perovskite oxides are considered as promising catalysts to activate PMS due to high structural stability and oxygen mobility (Lu et al., 2018; Miao et al., 2019; Rao et al., 2019). Perovskite oxides had a typical structural formula ABO_3, where the larger A-site cation was alkali-earth or rare-earth metal and the smaller B-site cation was 3d transition metal (Solís et al., 2017; Su et al., 2017). The properties of perovskite oxides could be easily modulated by substituting A- and B-sites with a foreign cation, changing the chemical composition or modifying the synthetic method (Lin et al., 2018; Zhu et al., 2014), and thus they were widely applied in chemistry and materials science communities. Especially, the investigations focused on the heterogeneous activation of PMS by iron-based perovskites have become a hotspot due to its environmentally benign and cost-effectiveness (Liu et al., 2018; Zhu et al., 2018a; Wang et al., 2019). For example, calcium substituted $LaFeO_{3-\delta}$ was an efficient catalyst to activate PMS for phenol degradation (Chu et al., 2018). Rao et al. (2018) evaluated the feasibility of $LaFeO_3$ for diclofenac degradation by activating PMS. Soltani et al. (2018) reported the complete degradation of bisphenol A by PMS activation with 10% Mn-doped $BiFeO_3$ nanoparticles. Duan et al. (2018) investigated the catalytic activity of $Pa_{0.5}Sr_{0.5}Co_{0.8}Fe_{0.2}O_{3-\delta}$ in the activation of PMS. To date, most strategies are the substitution of A or B cations in perovskite oxides with other metal elements for enhancing PMS activation, but this may be limited by the low solubility of some metal elements in materials processing.

Furthermore, the bulk perovskite oxides exhibited relatively low surface areas (below 30 m^2/g) even via metal doping modification, which strongly restricted their catalytic activities and industrial applications. To address this problem, the incorporation of support into perovskite oxides is an effective strategy. The physicochemical property and catalytic activity of catalysts were closely associated with the type and nature of the support used (Lin et al., 2019a; Rabelo-Neto et al., 2018; Wei et al., 2017; Yu et al., 2018), including large surface area, great oxygen mobility as well as conductivity. Moreover, the support materials have been used to immobilize cobalt- or palladium-based catalysts for enhancing PMS activation (Feng et al., 2018; Hu et al., 2019). Recently, some researchers have committed to the development of the supported perovskite catalysts in advanced oxidation process. For example, the degradation and mineralization of bisphenol F by $LaFeO_3$ in heterogeneous Fenton-like process could be improved due to the introduction of CeO_2 (Hammouda et al., 2017a). Lin et al. (2017) reported that zirconia-supported $LaCoO_3$ was a promising heterogeneous catalyst for activating PMS to degrade organic pollutants. However, to the best of our knowledge, the catalytic performance of the perovskite oxides supported on various supports for PMS activation has not been reported so far.

In this study, the $LaFeO_3$ perovskites supported on different supports (Al_2O_3, TiO_2, CeO_2, and SiO_2) by the citric sol-gel method were fabricated and applied for PMS activation. The selected supports were based on their stability against thermal treatment. The above catalysts were characterized by multiple techniques. Acid Orange 7 (AO7), a popular and non-biodegradable azo dye used widely in textile, pulp and paper industries, was served as target pollutant (Cheng et al., 2016; Shao et al., 2019; Wu et al., 2017a). Subsequently, $LaFeO_3/Al_2O_3$ was selected for further investigation due to its excellent catalytic activity. In addition, the stability of $LaFeO_3/Al_2O_3$ was also assessed.

2. Experimental section

2.1. Materials

Peroxymonosulfate triple salts (≥47% $KHSO_5$ basis), aluminum oxide (γ-Al_2O_3, 20 nm), and cerium nitrate ($Ce(NO_3)_3 \cdot 6H_2O$) was purchased from Sigma-Aldrich. Iron nitrate ($Fe(NO_3)_3 \cdot 9H_2O$), Lanthanum nitrate ($La(NO_3)_3 \cdot 6H_2O$), titanium dioxide (TiO_2, 20 nm), silicon oxide (SiO_2), 5, 5-Dimethyl-1-pyrroline N-oxide (DMPO), Acid Orange 7, methanol (MeOH), *tert*-butanol (TBA), dimethyl sulfoxide (DMSO), citric acid, and sodium thiosulfate were of analytical grade and purchased from Sinopharm Chemical Reagent Co., Ltd. All solutions were prepared using Milli-Q water (18.2 MΩ cm).

2.2. Preparation

CeO_2 was prepared according to the previous method (Zang et al., 2017). Prior to experiments, all supports (Al_2O_3, TiO_2, CeO_2, and SiO_2) were pretreated at 700 °C for 5.0 h in muffle furnace. 0.5 mM $La(NO_3)_3 \cdot 6H_2O$ and 0.5 mM $Fe(NO_3)_3 \cdot 9H_2O$ were added into 50 mL Milli-Q water under magnetic stirring 1.0 h. Then, citric acid was added into the above solution. The molar ratio of citric acid to total metal ions was 1:1. After stirring for 20 min, the support was added and mixed for 2.0 h. The loading of $LaFeO_3$ on the support was fixed at 20 wt%, referring to a number of literatures (Zhang et al., 2017; Zheng et al., 2017). The mixture was kept at 90 °C to evaporate water and then dried at 105 °C overnight. Finally, the obtained products were calcined at 700 °C (5 °C/min) for 5.0 h in a muffle furnace and were labeled as $LaFeO_3/CeO_2$, $LaFeO_3/SiO_2$, $LaFeO_3/Al_2O_3$, and $LaFeO_3/TiO_2$, respectively. For comparison, $LaFeO_3$ was also prepared.

2.3. Characterization

The morphologies of the samples were observed by a field emission scanning electron microscopy (FE-SEM, Hitachi S4800) equipped with energy dispersive spectrometers and a transmission electron microscopy (TEM, TecnaiG2 F20, FEI). Crystal structure was recorded by X-ray powder diffraction (XRD, Rigaku) with Cu Kα radiation. The specific surface area (SSA) and N_2 adsorption-desorption isotherms of the samples were measured at 77 K using an automated gas sorption analyzer (Autosorb-IQ, America). The samples were pre-degassed under vacuum at 200 °C for 2 h. X-ray photoelectron spectroscopy (XPS) was conducted on a photoelectron spectrometer (ESCALAB 250Xi, Thermo Fisher) with Al Kα as the X-ray source. All XPS spectra were calibrated to the C 1s peak at 284.8 eV. Raman spectra were obtained on a confocal micro-Raman spectrometer (Horiba Jobin Yvon LabRAM HR800) with an excitation of 633 nm laser light. The reducibility of supported $LaFeO_3$ perovskites was evaluated by hydrogen temperature-programmed reduction (H_2-TPR) using a ChemStar automated chemisorption analyzer (Quantachrome, American). Before measurement, the sample was treated at 400 °C for 2 h under N_2 atmosphere (5 °C/min). Subsequently, it was heated to 900 °C at a temperature ramp of 5 °C/min in 5% H_2/95% N_2 flow (90 mL/min). For O_2-TPD, the

samples were heated from 25 °C to 300 °C (10 °C/min) and kept for 30 min. After cooled down, the catalyst was purged with O_2 (30 mL/min) for 1 h. Then, it was heated up to 800 °C at a rate of 10 °C/min in a flow of N_2 (30 mL/min). Zeta potential of $LaFeO_3/Al_2O_3$ in solution (0.05 wt%) was measured by a zeta potential meter (Zetasizer Nano-ZS90, Malvern).

2.4. Experimental procedures

All experiments were performed in 250 mL sealed conical flask with a water bath (150 rpm, 25 °C). Typically, 10 mg catalyst and 0.25 mL of 200 mM PMS were simultaneously added to 100 mL AO7 solution with an initial concentration of 20 mg/L (without pH adjustment, initial pH 6.7) to start the reaction. At defined time intervals, 3.0 mL samples were withdrawn and filtered through 0.45 μm Millipore filter. Then, 30 μL of 30 mM sodium thiosulfate was added to quench the reaction for AO7 analysis. The effect of pH was investigated by adjusting solution pH using 0.1 M NaOH or H_2SO_4 rather than buffer salts, due to any avoidable complex reactions between free radicals and buffer species. Moreover, our preliminary test also showed that the AO7 degradation was significantly inhibited in the presence of 1.0 mM phosphate-buffered system at an identical pH value (Fig. S1 vs Fig. 6). After each cycle, the used catalysts were collected and washed with Milli-Q water several times and then dried in vacuum oven at 60 °C for reuse under an identical conditions. All experiments were carried out in triplicate and the standard deviations were reported. The degradation rates were calculated by the pseudo-first order kinetics equation:

$$\ln\left(\frac{C_t}{C_0}\right) = -K_{obs}t \quad (1)$$

where the C_0 and C_t were the concentration of AO7 at time 0 and t, respectively, t was reaction time (min), and K_{obs} was the apparent rate constant (min^{-1}).

2.5. Analytical methods

The concentration of AO7 was monitored by measuring the maximum absorbance at 485 nm using a Shimadzu UV-2550 spectrophotometer. Total organic carbon (TOC) was determined by a TOC-5050A analyzer. The contents of leached metal ions (La, Fe, Al, Si, Ce, and Ti) were detected by an inductively coupled plasma optical emission spectrometry (ICP-OES, PerkinElmer ICP 5300) (Wu et al., 2017b). The concentration of PMS was determined by a modified iodide spectrophotometry method (Liang et al., 2008). Electron spin resonance (ESR) experiments were conducted on a JES FA200 spectrometer with DMPO as the spin-trapping agent.

2.6. Electrochemical measurement

The electrochemical measurements of the samples were recorded by a standard three-electrode cell and CHI 760E workstation. A platinum plate electrode and a saturated calomel electrode were served as the counter electrode and reference electrode, respectively. The electrolyte was composed of 0.1 M Na_2SO_4 and 0.5 mM PMS. The working electrodes were prepared by dropping 10 μL of sample suspension (catalyst: 5 mg, DMF: 1.0 mL) onto a glassy carbon electrode to obtain a uniform film. Electrochemical impedance spectroscopy (EIS) was recorded at −0.3 V within the frequency range of 10^{-1}-10^5 Hz using an AC voltage amplitude of 5 mV.

3. Results and discussion

3.1. Characterization of catalysts

The XRD patterns of $LaFeO_3$ and supported $LaFeO_3$ perovskites were depicted in Fig. 1. For $LaFeO_3$, the diffraction peaks observed at 22.6°, 32.3°, 39.8°, 46.4°, 57.4°, 67.4° and 76.8° could be indexed to the (101), (121), (220), (202), (240), (242) and (204) planes of $LaFeO_3$ (JCPDS 37-1493), respectively, suggesting the formation of orthorhombic structure. All of supported $LaFeO_3$ exhibited characteristic diffraction peaks of $LaFeO_3$, besides $LaFeO_3/Al_2O_3$. As for $LaFeO_3/Al_2O_3$, only the peak of γ-Al_2O_3 was detected. This was mainly due to the penetration of $LaFeO_3$ into γ-Al_2O_3 pores, which in turn resulted in a higher dispersion. $LaFeO_3/Al_2O_3$ showed the lowest peak intensity, possibly owing to the poor crystallinity of γ-Al_2O_3. The crystal structures of anatase phase (JCPDS 12-1272) and rutile phase (JCPDS 21-1276) for TiO_2 were observed at $LaFeO_3/TiO_2$. In addition, the diffraction peaks of CeO_2 (JCPDS 34-0349) and SiO_2 (JCPDS 46-1045) were also identified for $LaFeO_3/CeO_2$ and $LaFeO_3/SiO_2$, respectively. For $LaFeO_3/SiO_2$, the highest diffraction peak at 26.7° was the (110) plane of quartz. Moreover, the characteristic diffraction peak intensity (32.3°) of $LaFeO_3$ on the support surface decreased in the order of $LaFeO_3 > LaFeO_3/SiO_2 > LaFeO_3/TiO_2 > LaFeO_3/CeO_2 > LaFeO_3/Al_2O_3$, which corresponded to the dispersion of $LaFeO_3$.

The specific surface area, pore volume and pore size of the supported $LaFeO_3$ perovskites were summarized in Table S1. The SSA of pure $LaFeO_3$ was 21.5 m^2/g, which was the typical SSA of $LaFeO_3$ prepared by citric sol gel method (Nie et al., 2015). The supported $LaFeO_3$ catalysts showed a higher SSA than pure $LaFeO_3$. Among them, $LaFeO_3/SiO_2$ reached the largest SSA of 139.6 m^2/g in comparison to 69.5 m^2/g, 72.9 m^2/g and 105.6 m^2/g for $LaFeO_3/TiO_2$, $LaFeO_3/CeO_2$ and $LaFeO_3/Al_2O_3$, respectively. Moreover, the addition of support increased total pore volume of catalysts, especially total pore volume of $LaFeO_3/Al_2O_3$ (0.34 cm^3/g) was 4.25 times than that of $LaFeO_3$. Additionally, the N_2 adsorption-desorption isotherms and corresponding pore size distributions were showed in Fig. S2. All catalysts exhibited type IV isotherm pattern with H3 hysteresis loops in the P/P_0 range of 0.6–1.0, indicating the characteristic of mesoporous structure. Besides $LaFeO_3/Al_2O_3$, the

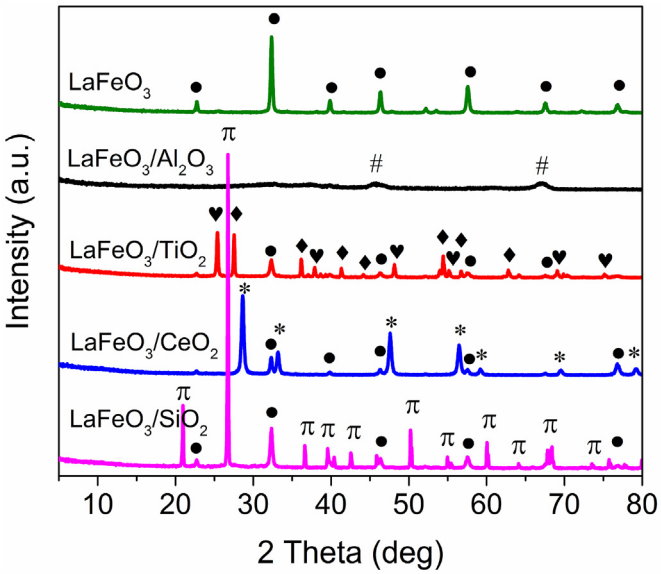

Fig. 1. XRD patterns of $LaFeO_3$, $LaFeO_3/Al_2O_3$, $LaFeO_3/TiO_2$, $LaFeO_3/CeO_2$, and $LaFeO_3/SiO_2$ (● −$LaFeO_3$; #−Al_2O_3; ♥ −Anatase TiO_2, ◆ −Rutile TiO_2; *−CeO_2; π−SiO_2).

supported $LaFeO_3$ catalysts kept a similar pore size distribution within 1.7−15 nm $LaFeO_3/Al_2O_3$ possessed a broader size distribution within 1.7−30 nm and mean pore size was 9.4 nm.

The morphologies of these catalysts were investigated using SEM. It could be obviously seen that $LaFeO_3$ formed irregular close-packed structures (Fig. 2a). The observed pores could be attributed to large quantities of gases emitted from the thermal decomposition of citric acid. The morphology and size of samples significantly changed as the support was added. For $LaFeO_3/Al_2O_3$, $LaFeO_3/TiO_2$ and $LaFeO_3/CeO_2$, spherical structures were both observed and particle sizes decreased from several micrometers to tens of nanometers as follow $LaFeO_3/Al_2O_3 > LaFeO_3/TiO_2 > LaFeO_3/CeO_2$ (Fig. 2b, c, d). $LaFeO_3/SiO_2$ showed a smooth surface with few small particles (Fig. 2f). The TEM image of $LaFeO_3/Al_2O_3$ was also provided in Fig. 3a. The average particle size of $LaFeO_3/Al_2O_3$ was estimated to be 30−40 nm and the rod-like particles of γ-Al_2O_3 were interconnected into the three dimensional porous structure. A high-resolution TEM revealed that these particles had lattice spacing of 0.27 nm, which corresponded with the interplanar spacing of the (121) plane of $LaFeO_3$ (Fig. 3c). The elemental mappings (Fig. 3d) and EDS analyses (Table S2) showed that $LaFeO_3$ were distributed uniformly on the Al_2O_3 surface and $LaFeO_3/Al_2O_3$ catalysts were successfully synthesized.

To study the reducibility of supported $LaFeO_3$ perovskites, H_2-TPR tests were carried out and the results are shown in Fig. S3. It could be seen that $LaFeO_3$ and $LaFeO_3/CeO_2$ showed three reduction peaks, while $LaFeO_3/SiO_2$, $LaFeO_3/TiO_2$ and $LaFeO_3/Al_2O_3$ showed two reduction peaks. La^{3+} ions did not take part in the reaction under H_2-TPR condition, so the observed reduction peaks were attributed to the reduction of iron ions and metal oxides. The reduction peaks occurred at low temperature (<550 °C) was ascribed to a two-step reduction of Fe^{4+} to Fe^{3+} and Fe^{3+} to Fe^{2+}, whereas the reduction of Fe^{2+} to Fe^0 occurred at high temperature (>550 °C). As for $LaFeO_3$, the second peak at 504 °C could be ascribed to the reduction of Fe^{3+} to Fe^{2+} and the third peak at 624 °C corresponded to the reduction of Fe^{2+} to Fe^0. For $LaFeO_3/SiO_2$ and $LaFeO_3/TiO_2$, the reduction peaks at low temperature almost disappeared and the related reduction peaks over 500 °C shifted toward higher temperature. The reduction of TiO_2 occurred at temperature higher than 600 °C, so the second reduction peak at 725 °C could be attributed to the reduction of Fe^{2+} and the reduction of TiO_2 (Ti^{4+}/Ti^{3+}). Meanwhile, the strong interaction between TiO_2 support and perovskite oxides resulted in higher reduction temperature (Giroir-Fendler et al., 2016). When Al_2O_3 was used as $LaFeO_3$ support, the reduction peak shifted to lower temperature (469 °C), suggesting that the incorporation of Al_2O_3 made it easier to be reduced. Moreover, the porous structure of γ-Al_2O_3 was more favorable for the diffusion of reactants to the nickel catalyst surface

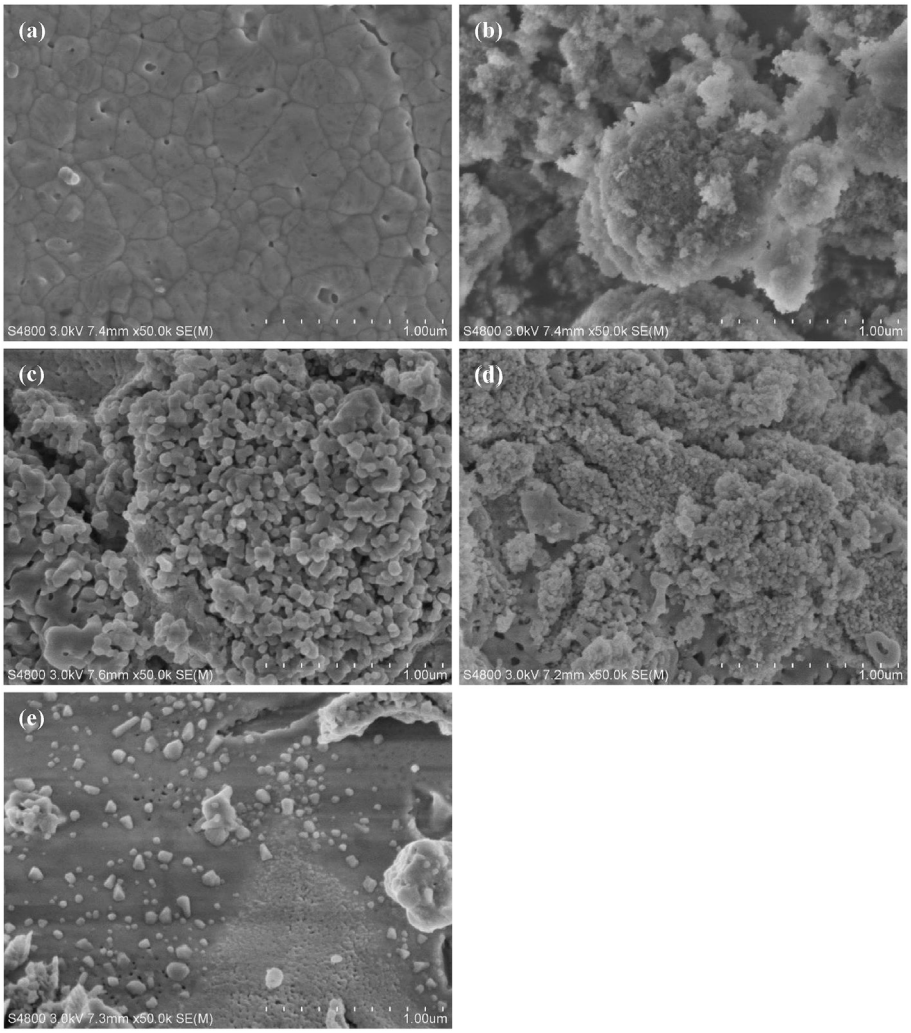

Fig. 2. SEM images of (a) $LaFeO_3$, (b) $LaFeO_3/Al_2O_3$, (c) $LaFeO_3/TiO_2$, (d) $LaFeO_3/CeO_2$, and (e) $LaFeO_3/SiO_2$.

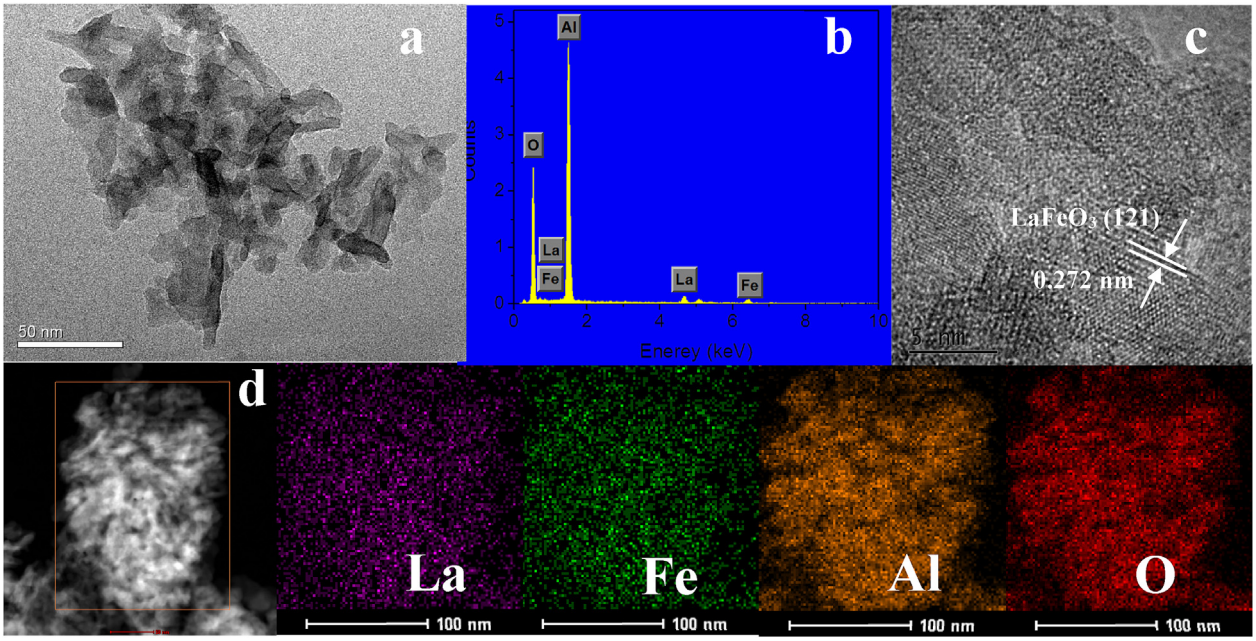

Fig. 3. TEM spectra (a), EDS spectra (b), HRTEM images (c), and SEM-EDS elemental mapping images (d) of $LaFeO_3/Al_2O_3$ composites.

compared to TiO_2 and SiO_2 (Pu et al., 2018). For $LaFeO_3/CeO_2$, the intensity of reduction peaks at low temperature increased and the position of reduction peaks shifted to the lowest temperature, which revealed the highest reducibility of $LaFeO_3/CeO_2$. The enhanced reducibility at low temperature could be attributed to the fact that the oxygen in the CeO_2 bulk could migrate to the surface immediately once surface oxygen was consumed, accelerating the mobility of lattice oxygen (Liu et al., 2013). Zheng et al. (2017) also observed that CeO_2 as $LaFeO_3$ support could facilitate the reducibility of nanocomposites at low temperature. In addition, a new reduction peak at 840 °C was present, corresponding to the reduction of bulk CeO_2.

XPS analyses were applied to investigate the surface element composition and chemical states of the supported $LaFeO_3$ perovskites. In addition to the common peaks of La, Fe and O, the peaks of Al, Ti, Ce and Si were observed from $LaFeO_3/Al_2O_3$, $LaFeO_3/TiO_2$, $LaFeO_3/CeO_2$ and $LaFeO_3/SiO_2$ (Fig. 4a), respectively. The high-resolution XPS spectrum of Al 2p, Ti 2p, Ce 3d and Si 2p were given in Fig. S4. The spectra of Al 2p (74.4 eV) and Si 2p (103.5 eV) from $LaFeO_3/Al_2O_3$ and $LaFeO_3/SiO_2$ indicated that these composites contained Al^{3+} and Si^{4+} species. In the Ti 2p spectra, the peaks at 458.3 eV and 464.0 eV could be ascribed to Ti $2p_{3/2}$ and Ti $2p_{1/2}$, respectively, suggesting the presence of Ti^{4+}. In the Ce 3d spectrum, eight characteristic peaks could be obtained. Among them, the peaks at 882.1 eV, 888.3 eV and 897.8 eV were corresponded to Ce $3d_{5/2}$, while the peaks at 900.5 eV, 907.1 eV and 916.3 eV were assigned to Ce $3d_{3/2}$, representing the existence of Ce^{4+} state. Additionally, the peaks at 884.2 eV and 902.8 eV were assigned to Ce^{3+} (Zang et al., 2017) and its content was determined to be 6.1%. Based on XPS quantitative analyses, the molar ratios of La/Fe on $LaFeO_3$, $LaFeO_3/Al_2O_3$, $LaFeO_3/TiO_2$, $LaFeO_3/CeO_2$ and $LaFeO_3/SiO_2$ were 0.99, 1.34, 2.19, 1.00 and 1.71, respectively (Table S2). This data was different from the EDS results, possibly due to analysis depth of XPS (≤10 nm). For $LaFeO_3$ and $LaFeO_3/CeO_2$, the La 3d spectrum could be deconvoluted into four peaks (Fig. 4b) The peaks at 833.8 eV and 850.6 eV were ascribed to La $3d_{5/2}$ and La $3d_{3/2}$, respectively, and the peaks at 837.8 eV and 855.1 eV were the corresponding shake-up satellites. The spin-orbit splitting of La 3d was 16.7−16.8 eV, suggesting the presence of La^{3+} (Hammouda et al., 2017b). Interestingly, for $LaFeO_3/Al_2O_3$, $LaFeO_3/TiO_2$ and $LaFeO_3/SiO_2$, the position of La 3d peaks shifted to higher binding energy and the shifted degree was in the order of $LaFeO_3/Al_2O_3 > LaFeO_3/SiO_2 > LaFeO_3/TiO_2$. Similar shift toward higher binding energies also occurred in the Fe 2p spectra (Fig. 4c), especially for $LaFeO_3/Al_2O_3$, which might suggest the increased Fe oxidation state or the decreased electron density (Xiao et al., 2015). Moreover, the peaks at 711.7 eV and 725.2 eV were assigned to Fe $2p_{3/2}$ and Fe $2p_{1/2}$, respectively, confirming the valence state of Fe^{3+} (Hammouda et al., 2017a). The spectra of O 1s could be deconvolved into two or three peaks (Fig. 4d). The binding energies at 529.2−529.8 eV, 531.0−531.4 eV and 532.5−533.0 eV were attributed to the lattice oxygen, surface absorbed oxygen and adsorbed molecular water, respectively (Zheng et al., 2017). The corresponding contents are summarized in Table S1. $LaFeO_3$ possessed lattice oxygen and surface adsorbed oxygen, of which the content of lattice oxygen reached the highest (62.3%). With the addition of support, the contents of lattice oxygen decreased as follow $LaFeO_3 > LaFeO_3/CeO_2 > LaFeO_3/TiO_2 > LaFeO_3/SiO_2 > LaFeO_3/Al_2O_3$. The incorporation of TiO_2 or CeO_2 into $LaFeO_3$ slightly decreased the content of lattice oxygen. However, the lattice oxygen content of $LaFeO_3/SiO_2$ obviously decreased to 25.1%, while the adsorbed molecular water increased to 46.3%. More interestingly, the lattice oxygen for $LaFeO_3/Al_2O_3$ could not be observable and surface absorbed oxygen was predominant with 94.4%.

In order to gain insight into the active oxygen species of the above catalysts, O_2-TPD tests were conducted. As shown in Fig. 5, the first desorption peak lower than 200 °C was ascribed to the physically adsorbed oxygen and the second peak at 200−600 °C was attributed to the chemisorbed surface-active oxygen. The third desorption peak over 600 °C was assigned to lattice oxygen (Xiao et al., 2015). $LaFeO_3$ and $LaFeO_3/TiO_2$ both exhibited two similar desorption peaks. Three desorption peaks could be observed at $LaFeO_3/CeO_2$ (124 °C, 387 °C and 441 °C) and its peak intensity at low temperature was higher, indicating better oxygen mobility. The desorption peak of $LaFeO_3/SiO_2$ could be almost invisible. However, $LaFeO_3/Al_2O_3$ showed the highest peak intensity than $LaFeO_3$ and

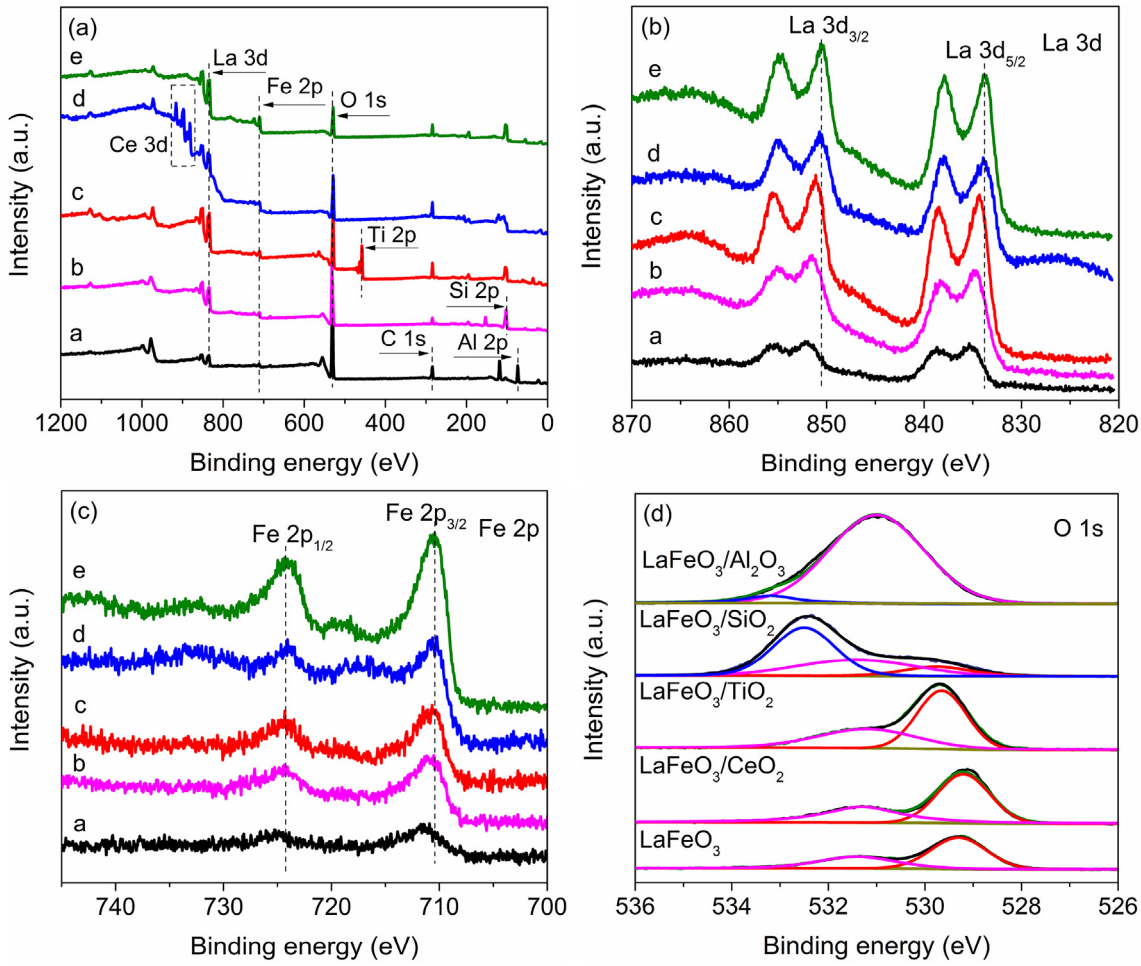

Fig. 4. XPS spectra of the $LaFeO_3$ perovskites catalysts. (a) XPS survey scan spectrum; high-resolution XPS spectrum of (b) La 3d, (c) Fe 2p, and (d) O 1s (a–$LaFeO_3/Al_2O_3$; b–$LaFeO_3/SiO_2$; c–$LaFeO_3/TiO_2$; d–$LaFeO_3/CeO_2$; e–$LaFeO_3$).

other supported $LaFeO_3$. In addition, the desorption peak within 200–600 °C shifted toward lower temperature, which could be explained by the high SSA of Al_2O_3 (Zhang et al., 2017). As known, the catalytic activity of catalysts in the oxidation reaction mainly depended on the chemisorbed surface-active oxygen at a relatively low temperature (Xu and Wang, 2012). Therefore, $LaFeO_3/Al_2O_3$ possessed the largest amounts of chemisorbed surface-active oxygen, possibly suggesting its excellent catalytic performance for PMS activation.

3.2. Heterogeneous catalytic activity of catalysts

The catalytic performances of the $LaFeO_3$ catalysts supported on the various supports for PMS activation were investigated. As first, their adsorption without adding PMS was evaluated and the results are displayed in Fig. 6a. Besides $LaFeO_3/Al_2O_3$, less than 11% of AO7 was removed within 120 min. The adsorption removal was 20.4% by $LaFeO_3/Al_2O_3$, which might attribute to high SSA and pore volume. Subsequently, the degradation of AO7 by combination of catalysts and PMS was carried out (Fig. 6b). The AO7 removal by PMS alone was 26.1%. In comparison to PMS alone, the presence of support showed an insignificant effect on AO7 degradation (Fig. S5), indicating a negligible catalytic activity of supports. In contrast, the catalytic efficiencies of $LaFeO_3$ over different supports enhanced as

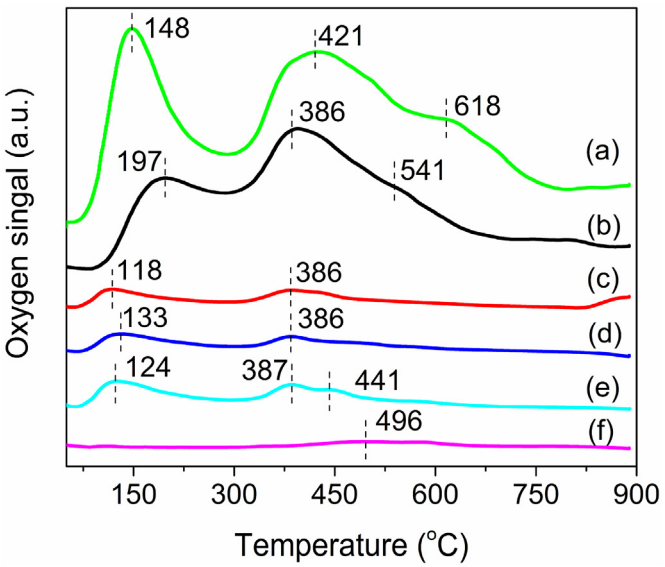

Fig. 5. O_2-TPD profiles of Al_2O_3 (a), $LaFeO_3/Al_2O_3$ (b), $LaFeO_3$ (c), $LaFeO_3/TiO_2$ (d), $LaFeO_3/CeO_2$ (e) and $LaFeO_3/SiO_2$ composites (f).

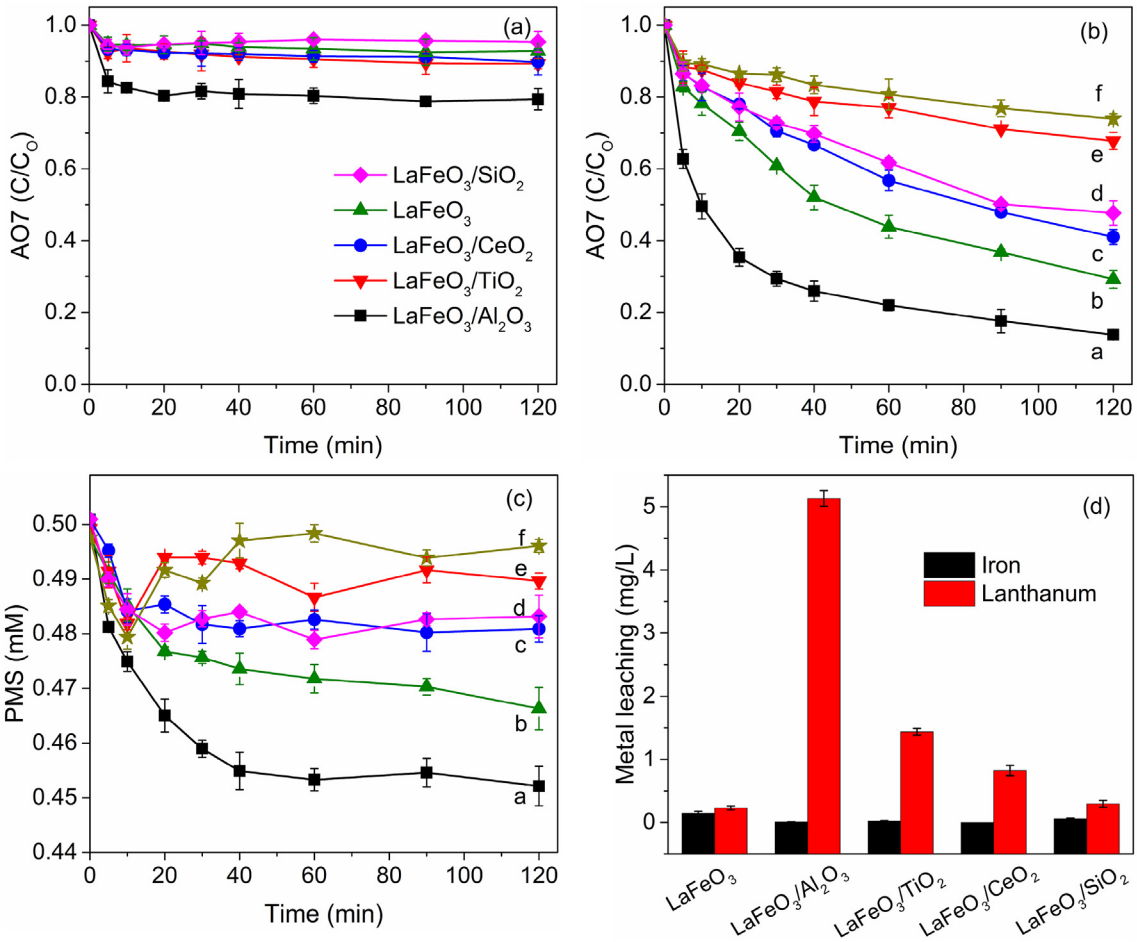

Fig. 6. The removal of AO7 by different $LaFeO_3$ perovskites in the (a) absence or (b) presence of PMS (a–$LaFeO_3/Al_2O_3$; b–$LaFeO_3$; c–$LaFeO_3/CeO_2$; d–$LaFeO_3/SiO_2$; e–$LaFeO_3/TiO_2$; f–PMS alone), (c) the decomposition of PMS, (d) the leaching of metal ions in the corresponding PMS processes. Condition: [AO7] = 20 mg/L, [PMS] = 0.5 mM, [catalysts] = 0.1 g/L, without pH adjustment.

follow: $LaFeO_3/Al_2O_3$ (86.2%) > $LaFeO_3$ (70.8%) > $LaFeO_3/CeO_2$ (59.0%) > $LaFeO_3/SiO_2$ (52.3%) > $LaFeO_3/TiO_2$ (32.2%). To evaluate the reaction rates of the above catalysts, the pseudo first-order kinetics constants were employed and the related rate constants are listed in Table 1. AO7 degradation by these catalysts followed pseudo first-order kinetics well. The rate constant for $LaFeO_3/Al_2O_3$ was calculated to be the highest (0.03129 min^{-1}), which was 3.2 times than that for $LaFeO_3$. Moreover, the related TOC removal was compared. Among these catalysts, $LaFeO_3/Al_2O_3$ showed the highest mineralization ability with the efficiency of 56.5% (Table 1), while the mineralization ability of other supported $LaFeO_3$ catalysts was even lower than that of $LaFeO_3$, demonstrating the superiority of Al_2O_3 as perovskite support. Hou et al. (2018) also found that supported N-doped carbon quantum dots on Al_2O_3 exhibited much higher activity for persulfate activation than other supported catalysts. Li et al. (2016) reported that the addition of SiO_2 could not only increase the dispersion of $LaFeO_3$, but also effectively absorbed dyes from solution to pores and subsequently transported to the $LaFeO_3$ oxidation. Hence, the adsorbed AO7 into $LaFeO_3/Al_2O_3$ catalyst was favorable to promoting AO7 degradation. It is noteworthy that $LaFeO_3/SiO_2$ has the highest SSA while its degradation efficiency was much less than $LaFeO_3/Al_2O_3$, which suggests that other key factors contribute to the AO7 degradation. Hammouda et al. (2017b) also reported that the catalytic activity of perovskite for PMS activation was not positively correlated with the SSA.

Electrochemical measurement was employed to assess the charge transfer process on different supported $LaFeO_3$ catalysts. It was reported that the semicircle diameter occurred at high frequency region corresponded to electron transfer process, while it corresponded to mass transfer process at low frequency region (Gao et al., 2014). Evidently, $LaFeO_3/Al_2O_3$ exhibited a lower semicircle diameter than other catalysts (Fig. S6), indicating faster electron transfer. Based on the above characterization analysis and discussion, Al_2O_3 as the $LaFeO_3$ support displayed excellent catalytic activity for PMS activation among these catalysts, which was attributed to its large surface area, suitable redox property, abundant chemisorbed surface-active oxygen, and faster electron transfer.

Meanwhile, the decomposition of PMS was monitored in the above processes (Fig. 6c). The result further indicated that $LaFeO_3$/

Table 1
The pseudo-first order rate constants and TOC removal by PMS, $LaFeO_3$, and supported $LaFeO_3$ perovskites.

Catalyst	K_{obs} (min^{-1})	R^2	TOC removal (%)
$LaFeO_3/Al_2O_3$	0.0313	0.868	56.5%
$LaFeO_3/TiO_2$	0.0027	0.809	8.1%
$LaFeO_3/CeO_2$	0.0070	0.971	28.4%
$LaFeO_3/SiO_2$	0.0058	0.952	26.3%
$LaFeO_3$	0.0097	0.952	40.7%
PMS	0.0019	0.809	2.3%

Al_2O_3 was the most effective catalyst for PMS activation, which was also matched with AO7 degradation. After reaction, the leaching of iron and lanthanum ions from catalysts was measured using ICP-OES (Fig. 6d). The leached amount of La^{3+} from $LaFeO_3/Al_2O_3$ reached the highest (5.13 mg/L). It has reported that La^{3+} may react with PMS to accelerate the reaction (Lin et al., 2017). Under the same condition, the degradation efficiency only enhanced 9.8% by adding 10.0 mg/L La^{3+} (maximum leaching concentration) in comparison with PMS oxidation (Fig. S7), suggesting that the reaction mainly occurred at the $LaFeO_3/Al_2O_3$ surface. Moreover, the incorporation of support significantly decreased the leached iron ions. Especially, the iron leaching (0.007 mg/L) from $LaFeO_3/Al_2O_3$ was 20 times lower than that from $LaFeO_3$. According to previous report, Fe^{2+}/Fe^{3+} were responsible for the generation of ·OH and $SO_4^{\bullet-}$ (Wu et al., 2018a), but its concentration released from $LaFeO_3/Al_2O_3$ was not enough to activate PMS. Therefore, $LaFeO_3/Al_2O_3$ was considered as the most effective catalyst for AO7 degradation and was selected for further investigation.

3.3. Effect of pH

In heterogeneous catalytic PMS reaction, the solution pH was an important parameter that could affect the interfacial interactions between organic pollutants, PMS and catalysts (He et al., 2017; Chen et al., 2018). As illustrated in Fig. 7a, the degradation of AO7 decreased with the increase of pH and drastically decreased as pH went above 9.0. More specifically, the degradation efficiency was 96.7% at pH 3.0 while only 47.3% at pH 11.0 after 120 min reaction. This could be explained by the following reasons. First, the AO7 molecule had two pKa values ($pK_{a1} = 1.1$ and $pK_{a2} = 11.0$) and only negatively charged mono-anion form existed in the aqueous solution within pH range of 2.0–9.6 (Bandara et al., 2006). The pH_{pzc} of $LaFeO_3/Al_2O_3$ was determined to be 9.5 (Fig. S8). Consequently, $LaFeO_3/Al_2O_3$ surface was negatively charged when the solution pH was above pH_{pzc}, which could decrease the adsorbed amount of AO7 on the catalyst surface and degradation efficiency. Second, pH could affect the relative amounts of PMS species whose pK_{a1} and pK_{a2} were 0 and 9.4, respectively, so HSO_5^- was the main species within pH range of 3.0–9.0. As the pH increased over 9.0, the electrostatic repulsion existed, which was not favor for the AO7 degradation. Although base could activate PMS to produce reactive species (Qi et al., 2016), but the enhanced degradation was not observed in this study. Third, the solution pH also affected the leaching of metal ions from $LaFeO_3/Al_2O_3$ (Fig. 7b). The leaching of lanthanum (7.50 mg/L), iron (1.20 mg/L) and aluminum (2.44 mg/L) reached the highest when initial pH was 3.0. With the increase of pH, the leached iron was almost not observable and the leaching of lanthanum and aluminum decreased. Especially, the leached lanthanum and aluminum were only 0.600 mg/L and 0.195 mg/L at pH 11.0, respectively. These results were well consistent with the report that acidic pH promoted contaminants degradation and the leaching of metal ions (Hammouda et al., 2017b).

3.4. Mechanistic studies

It is generally accepted that ·OH and $SO_4^{\bullet-}$ are considered to be the predominant reactive species during PMS activation process. Firstly, ESR technology was used to *in-situ* examine the generation of $SO_4^{\bullet-}$ and ·OH. No signals of radicals were detected when PMS was present in the AO7 solution (Fig. 8a), indicating that PMS itself could not decompose to produce free radicals. In the $LaFeO_3/Al_2O_3$-PMS process, the characteristic signals of DMPO-OH and DMPO-SO_4 were identified based on their hyperfine splitting constants (DMPO-OH, aH = 15.0 G and aN = 14.9 G; DMPO-SO_4, aN = 13.7 G, aH = 10.0 G, aH = 1.41 G, and aH = 0.78 G), which was in

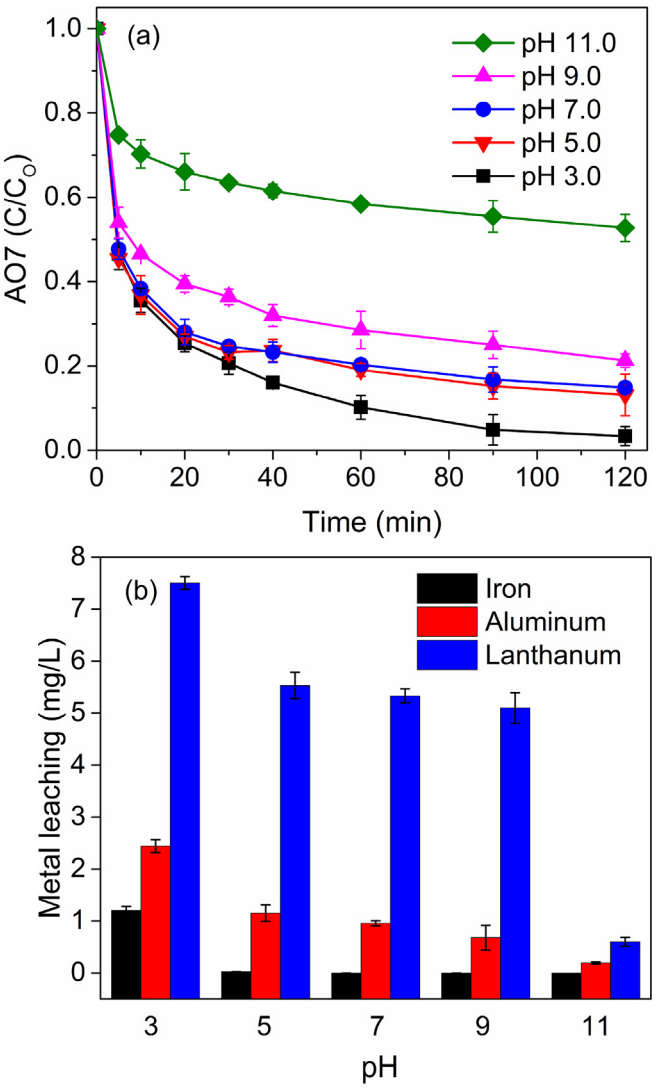

Fig. 7. Effects of solution pH on AO7 degradation (a) and the leached metal ions (b). Condition: [AO7] = 20 mg/L, [PMS] = 0.5 mM, [$LaFeO_3/Al_2O_3$] = 0.1 g/L.

accordance with our previous study using ferrate(VI) as PMS activator (Wu et al., 2018b). In the presence of substrate AO7, signal intensity of DMPO-OH increased continuously as the reaction proceeded, while signal intensity of DMPO-SO_4 increased in the first 10 min and then decreased slightly (Fig. 8b). Moreover, signal intensity of DMPO-SO_4 was much lower than signal intensity of DMPO-OH. Possible reason included continuous consumption of $SO_4^{\bullet-}$ for AO7 degradation and relatively stronger trapping ability of DMPO for ·OH (Lin et al., 2019b; Zhu et al., 2018b). However, in the absence of AO7, the relative intensities of $SO_4^{\bullet-}$ and ·OH was much lower, as also mirrored by PMS decomposition (Fig. S9), and thus implied that the presence of AO7 could accelerate PMS activated by $LaFeO_3/Al_2O_3$. Furthermore, the signal intensity in $LaFeO_3/Al_2O_3$-PMS process was higher than that in $LaFeO_3$-PMS process, which was well consistent with the degradation result.

To evaluate the contribution of ·OH and $SO_4^{\bullet-}$ in the $LaFeO_3/Al_2O_3$-PMS process, classical quenching tests using MeOH and TBA as quenching agents were carried out. MeOH was used to effectively capture both $SO_4^{\bullet-}$ ($0.9–1.3 \times 10^7\ M^{-1}\ s^{-1}$) and ·OH ($8.0–10 \times 10^8\ M^{-1}\ s^{-1}$), while TBA was effective for ·OH barely ($k_{OH} = 3.8–7.6 \times 10^8\ M^{-1}\ s^{-1}$, $k_{SO4\cdot-} = 4.0–9.1 \times 10^5\ M^{-1}\ s^{-1}$)

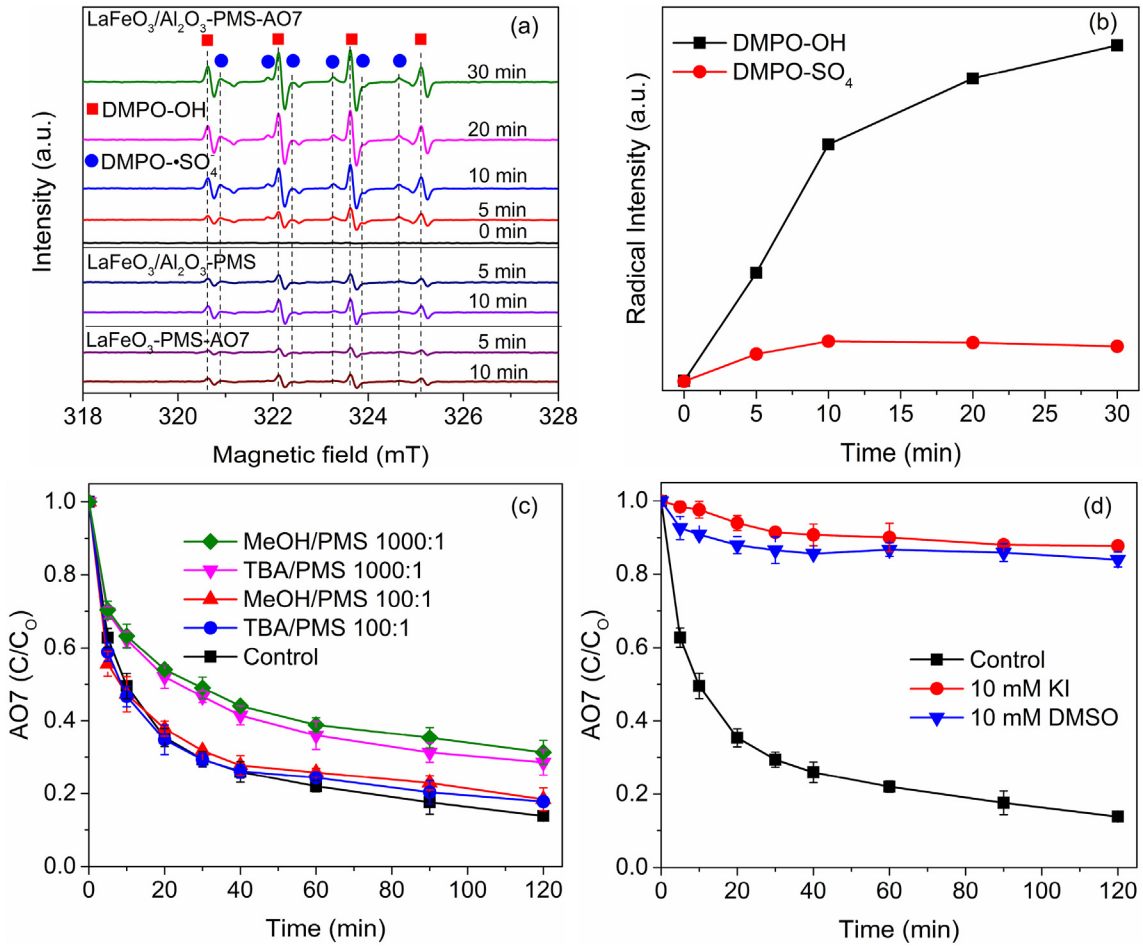

Fig. 8. Spin-trapping EPR spectra (a) and radical evolution (b) in $LaFeO_3/Al_2O_3$-PMS process, effects of methanol and *tert*-butanol (c) and KI and DMSO (d) on AO7 degradation in $LaFeO_3/Al_2O_3$-PMS process. Condition: [AO7] = 20 mg/L, [PMS] = 0.5 mM, [$LaFeO_3/Al_2O_3$] = 0.1 g/L, [DMPO] = [TEMP] = 100 mM, without pH adjustment.

(Eibenberger et al., 1978). As showed in Fig. 8c, the negligible effects on AO7 degradation could be observed at molar ratio 100:1 of quenching agents. As further increase molar ratio of TBA/PMS to 1000:1, the degradation efficiency was only decreased by 16.1%. MeOH at an identical molar ratio also did not show a stronger inhibitory effect, which might due to that the hydrophilic MeOH was difficult to eliminate surface-bound radicals effectively. To determine the occurrence of surface-bound radicals, potassium iodide (KI) and dimethyl sulfoxide (DMSO) was used because they could capture surface-bound radicals (Xu and Wang, 2012; Yao et al., 2017). On this occasion, AO7 degradation was almost completely inhibited. Both degradation efficiencies were even lower than the adsorption efficiency by $LaFeO_3/Al_2O_3$ alone (Fig. 8d), which might be attributed to the fact that the presence of KI or DMSO also affected the surface adsorption sites of $LaFeO_3/Al_2O_3$. A similar phenomenon was also observed in the PMS activated by $ZnCo_2O_4$ catalyst (Hu et al., 2018a). To further assess the role of heterogeneous reaction, we conducted the experiment that $LaFeO_3/Al_2O_3$ catalyst was dispersed in the AO7 solution, intensely stirred for 120 min and separated to obtain the filtrate, and then desired amount of PMS were added to trigger the reaction. The degradation efficiency of AO7 was only 23.1% (Fig. S9), which confirmed that the AO7 degradation mainly occurred at the $LaFeO_3/Al_2O_3$ surface. Furthermore, nitrobenzene was served as probe compound for ·OH because it was reactive toward ·OH ($3.9 \times 10^9\ M^{-1}\ s^{-1}$) but resistant to $SO_4^{\bullet-}$ (Guan et al., 2013). Nitrobenzene was removed hardly in the $LaFeO_3/Al_2O_3$-PMS process (Fig. S10) even when the concentration of nitrobenzene was set at 1.0 mg/L. Compared with AO7 degradation, the degradation of nitrobenzene could be negligible. However, the presence of benzoic acid remarkably inhibited the AO7 degradation (Fig. S11), which confirmed the key role of $SO_4^{\bullet-}$ since benzoic acid was commonly used as $SO_4^{\bullet-}$ scavenger. Based on the above results, $SO_4^{\bullet-}$ and ·OH are both involved in the $LaFeO_3/Al_2O_3$-PMS process, whereas surface-bound $SO_4^{\bullet-}$ is the predominant reactive species.

To obtain insights into the activation mechanism of PMS, $LaFeO_3/Al_2O_3$ before and after reactions were characterized by XPS techniques. After reaction, a new N 1s peak was observed on the XPS survey spectrum and peak intensity of C 1s was significantly increased (Fig. S12), indicating AO7 and its intermediates were adsorbed on the catalyst surface. In section 3.1, we have confirmed the presence of La^{3+} and Fe^{3+} on $LaFeO_3/Al_2O_3$. The peak intensity of La 3d remarkably decreased after reaction, which was ascribed to the leached La^{3+}. Observed from high-resolution XPS spectra of Fe 2p, the characteristic peak of Fe(III) assigned to 711.7 eV and 725.2 eV could be obtained, while that of Fe(II) was hardly detected. Nevertheless, the binding energies of Fe $2p_{3/2}$ and Fe $2p_{1/2}$ shifted to a higher binding energies (712.3 eV and 725.5 eV) after reaction, which might suggest the redox couples of Fe(II)/Fe(III). Similar shift toward high binding energy of Fe 2p was also reported in the surface-active bismuth ferrite/PMS process (Oh et al., 2017). In addition, the relative contents of surface absorbed oxygen

decreased from 94.1% to 87.8% after reaction, indicating that it involved in the reaction, which further proved the role of chemisorbed surface-active oxygen.

Based on experiment results and previous literatures (Khan et al., 2019; Hu et al., 2018b), possible degradation mechanisms of AO7 by PMS activation using $LaFeO_3/Al_2O_3$ were illustrated as follow. Firstly, a certain amount of AO7 molecules in solution was adsorbed on $LaFeO_3/Al_2O_3$ surface. Secondly, surface-bound $SO_4^{\bullet-}$ radicals could be formed on the catalyst surface via the redox reaction of Fe(II)/Fe(III). Thirdly, adsorbed AO7 molecules were *in-situ* degraded by surface-bound $SO_4^{\bullet-}$ and released free active sites. Lastly, the above reactions were started again and continued until all the AO7 was removed.

$$\equiv Fe^{3+} - OH + HSO_5^- \rightarrow \equiv Fe^{3+} - SO_5^- + H_2O \quad (2)$$

$$\equiv Fe^{3+} - SO_5^- + H_2O \rightarrow \equiv Fe^{2+} - OH + SO_5^{\bullet-} + H^+ \quad (3)$$

$$\equiv Fe^{2+} - OH + HSO_5^- \rightarrow \equiv Fe^{2+} - SO_5^- + H_2O \quad (4)$$

$$\equiv Fe^{2+} - SO_5^- + H_2O \rightarrow \equiv Fe^{3+} - OH + SO_4^{\bullet-} + OH^- \quad (5)$$

3.5. Reusability of $LaFeO_3/Al_2O_3$ catalyst

The recyclability of $LaFeO_3/Al_2O_3$ catalyst for AO7 degradation was evaluated by five consecutive tests. As observed in Fig. 9, degradation efficiency of AO7 remained almost unchanged in the first two cycles. After three cycles, $LaFeO_3/Al_2O_3$ exhibited degradation efficiency of 73.4%, which was comparable to that of fresh $LaFeO_3$, and the degradation efficiency could still reach 67.4% in the fifth cycle. In contrast, the catalytic ability of $LaFeO_3$ in the successive cycle was significantly decreased, with an efficiency of 24.4% after five cycles. The decreased efficiency might be due to the unavoidable leaching loss of catalyst and the blockage of surface active sites by AO7 and its degradation intermediates, as also confirmed by XPS result. The stability of $LaFeO_3/Al_2O_3$ was further examined by SEM and XRD patterns (Figs. S13 and S14), which showed no obvious changes of the morphological and crystal structures after reaction. Hence, the catalytic activity and stability of $LaFeO_3$ were greatly improved due to the incorporation of Al_2O_3, which also further confirmed that $LaFeO_3/Al_2O_3$ possessed satisfying catalytic activity after used for five cycles.

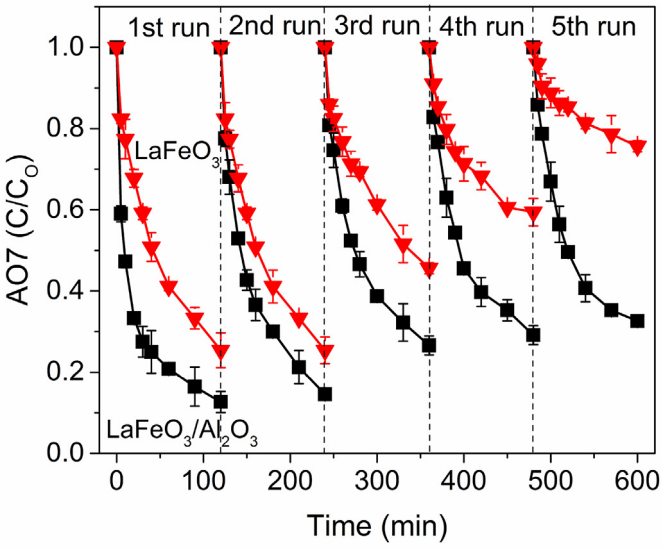

Fig. 9. The stability of $LaFeO_3$ and $LaFeO_3/Al_2O_3$ composites. Condition: [AO7] = 20 mg/L, [PMS] = 0.5 mM, [catalysts] = 0.1 g/L, without pH adjustment.

4. Conclusions

In the present study, a series of $LaFeO_3$ catalysts supported on various supports were prepared by the citric sol-gel method and their catalytic activities toward PMS activation were evaluated through AO7 degradation. The following conclusions were drawn:

1. The incorporation of supports affected the textural and chemical properties of $LaFeO_3$ catalysts significantly.
2. Among $LaFeO_3$ catalysts studied, $LaFeO_3$ supported on Al_2O_3 possessed the highest catalytic and mineralization ability, due to large surface area, abundant chemisorbed surface-active oxygen, suitable redox property, and faster electron transfer.
3. AO7 degradation followed the pseudo first-order kinetics and the rate constant of $LaFeO_3/Al_2O_3$ for AO7 degradation was 3.2 times that of $LaFeO_3$.
4. Hydroxyl and sulfate radicals were produced on $LaFeO_3/Al_2O_3$ surface, while sulfate radicals were the main reactive species.
5. Mechanisms for PMS activation by $LaFeO_3/Al_2O_3$ were proposed.

Acknowledgements

This work was supported by the project of National Natural Science Foundation of China (Grant No.: 51478172 and 51521006), the International S&T Cooperation Program of China (Contract No.: 2015DFG92750), the Department of Science and Technology of Guangdong Province of China (Contract No.:2018S0011)and the Department of Science and Technology of Hunan Province of China (Contract No.: 2017JJ2029 and 2017SK2362).

Appendix A. Supplementary data

Supplementary data to this article can be found online at https://doi.org/10.1016/j.chemosphere.2019.124478.

References

Bandara, J., Mielczarski, J.A., Kiwi, J., 2006. Molecular mechanism of surface recognition. Azo dyes degradation on Fe, Ti, and Al oxides through metal sulfonate complexes. Langmuir 15, 7670–7679.
Cheng, Y., He, H., Yang, C., Zeng, G., Li, X., Chen, H., Yu, G., 2016. Challenges and solutions for biofiltration of hydrophobic volatile organic compounds. Biotechnol. Adv. 34, 1091–1102.
Chen, Y., He, H., Liu, H., Li, H., Zeng, G., Xia, X., Yang, C., 2018. Effect of salinity on removal performance and activated sludge characteristics in sequencing batch reactors. Bioresour. Technol. 249, 890–899.
Chu, Y., Tan, X., Shen, Z., Liu, P., Han, N., Kang, J., Duan, X., Wang, S., Liu, L., Liu, S., 2018. Efficient removal of organic and bacterial pollutants by Ag-$La_{0.8}Ca_{0.2}Fe_{0.94}O_{3-\delta}$ perovskite via catalytic peroxymonosulfate activation. J. Hazard Mater. 356, 53–60.
Duan, X., Su, C., Miao, J., Zhong, Y., Shao, Z., Wang, S., Sun, H., 2018. Insights into perovskite-catalyzed peroxymonosulfate activation: maneuverable cobalt sites for promoted evolution of sulfate radicals. Appl. Catal. B Environ. 220, 626–634.
Eibenberger, H., Steenken, S., O'Neill, P., Schultefrohlinde, D., 1978. Pulse radiolysis and electron spin resonance studies concerning the reaction of $SO_4^{\bullet-}$ with alcohols and ethers in aqueous solution. J. Phys. Chem. 82, 749–750.
Feng, Y., Li, H., Wu, D., Liao, C., Fan, Y., Lee, P., Shih, K., 2018. Supported palladium nanoparticles as highly efficient catalysts for radical production: support-dependent synergistic effects. Chemosphere 207, 27–32.
Gao, M., Sheng, W., Zhuang, Z., Fang, Q., Gu, S., Jiang, J., Yan, Y., 2014. Efficient water oxidation using nanostructured α-nickel-hydroxide as an electrocatalyst. J. Am. Chem. Soc. 136, 7077–7084.
Giroir-Fendler, A., Alves-Fortunato, M., Richard, M., Wang, C., Díaz, J.A., Gil, S., Zhang, C., Can, F., Bion, N., Guo, Y., 2016. Synthesis of oxide supported $LaMnO_3$ perovskites to enhance yields in toluene combustion. Appl. Catal. B Environ. 180, 29–37.
Guan, Y.H., Ma, J., Ren, Y.M., Liu, Y.L., Xiao, J.Y., Lin, L.Q., Zhang, C., 2013. Efficient

degradation of atrazine by magnetic porous copper ferrite catalyzed peroxymonosulfate oxidation via the formation of hydroxyl and sulfate radicals. Water Res. 47, 5431–5438.
Hammouda, S.B., Zhao, F., Safaei, Z., Babu, I., Ramasamy, D.L., Sillanpää, M., 2017a. Reactivity of novel ceria–perovskite composites CeO_2-$LaMO_3$ (MCu, Fe) in the catalytic wet peroxidative oxidation of the new emergent pollutant 'Bisphenol F': characterization, kinetic and mechanism studies. Appl. Catal. B Environ. 218, 119–136.
Hammouda, S.B., Zhao, F., Safaei, Z., Srivastava, V., Lakshmi Ramasamy, D., Iftekhar, S., kalliola, S., Sillanpää, M., 2017b. Degradation and mineralization of phenol in aqueous medium by heterogeneous monopersulfate activation on nanostructured cobalt based-perovskite catalysts $ACoO_3$ (A=La, Ba, Sr and Ce): characterization, kinetics and mechanism study. Appl. Catal. B Environ. 215, 60–73.
He, H., Chen, Y., Li, X., Cheng, Y., Yang, C., Zeng, G., 2017. Influence of salinity on microorganisms in activated sludge processes: a review. Int. Biodeterior. Biodegrad. 119, 520–527.
Hou, J., Li, H., Tang, Y., Sun, J., Fu, H., Qu, X., Xu, Z., Yin, D., Zheng, S., 2018. Supported N-doped carbon quantum dots as the highly effective peroxydisulfate catalysts for bisphenol F degradation. Appl. Catal. B Environ. 238, 225–235.
Hu, L., Zhang, G., Liu, M., Wang, Q., Dong, S., Wang, P., 2019. Application of nickel foam-supported Co_3O_4-Bi_2O_3 as a heterogeneous catalyst for BPA removal by peroxymonosulfate activation. Sci. Total Environ. 647, 352–361.
Hu, L., Zhang, G., Liu, M., Wang, Q., Wang, P., 2018a. Optimization of the catalytic activity of a $ZnCo_2O_4$ catalyst in peroxymonosulfate activation for bisphenol A removal using response surface methodology. Chemosphere 212, 152–161.
Hu, L., Zhang, G., Liu, M., Wang, Q., Wang, P., 2018b. Enhanced degradation of Bisphenol A (BPA) by peroxymonosulfate with Co_3O_4-Bi_2O_3 catalyst activation: effects of pH, inorganic anions, and water matrix. Chem. Eng. J. 338, 300–310.
Hu, P., Long, M., 2016. Cobalt-catalyzed sulfate radical-based advanced oxidation: a review on heterogeneous catalysts and applications. Appl. Catal. B Environ. 181, 103–117.
Ji, Y., Dong, C., Kong, D., Lu, J., Zhou, Q., 2015. Heat-activated persulfate oxidation of atrazine: implications for remediation of groundwater contaminated by herbicides. Chem. Eng. J. 263, 45–54.
Khan, M., Klu, P., Wang, C., Zhang, W., Luo, R., Zhang, M., Qi, J., Sun, X., Wang, L., Li, J., 2019. Metal-organic framework-derived hollow Co_3O_4/carbon as efficient catalyst for peroxymonosulfate activation. Chem. Eng. J. 363, 234–246.
Li, H., Zhu, J., Xiao, P., Zhan, Y., Lv, K., Wu, L., Li, M., 2016. On the mechanism of oxidative degradation of rhodamine B over $LaFeO_3$ catalysts supported on silica materials: role of support. Microporous Mesoporous Mater. 221, 159–166.
Liang, C., Huang, C., Mohanty, N., Kurakalva, R.M., 2008. A rapid spectrophotometric determination of persulfate anion in ISCO. Chemosphere 73, 1540–1543.
Lin, K.A., Chen, Y.C., Lin, T.Y., Yang, H., 2017. Lanthanum cobaltite perovskite supported on zirconia as an efficient heterogeneous catalyst for activating Oxone in water. J. Colloid Interface Sci. 497, 325–332.
Lin, Y., Wu, S., Li, X., Wu, X., Yang, C., Zeng, G., Peng, Y., Zhou, Q., Lu, L., 2018. Microstructure and performance of Z-scheme photocatalyst of silver phosphate modified by MWCNTs and Cr-doped $SrTiO_3$ for malachite green degradation. Appl. Catal. B Environ. 227, 557–570.
Lin, Y., Wu, S., Yang, C., Chen, M., Li, X., 2019a. Preparation of size-controlled silver phosphate catalysts and their enhanced photocatalysis performance via synergetic effect with MWCNTs and PANI. Appl. Catal. B Environ. 245, 71–86.
Lin, Y., Wu, X., Han, Y., Yang, C., Ma, Y., Du, C., Teng, Q., Liu, H., Zhong, Y., 2019b. Spatial separation of photogenerated carriers and enhanced photocatalytic performance on Ag_3PO_4 catalysts via coupling with PPy and MWCNTs. Appl. Catal. B: Environ. 258, 117969.
Liu, Y., Dai, H., Deng, J., Li, X., Wang, Y., Arandiyan, H., Xie, S., Yang, H., Guo, G., 2013. Au/3DOM $La_{0.6}Sr_{0.4}MnO_3$: highly active nanocatalysts for the oxidation of carbon monoxide and toluene. J. Catal. 305, 146–153.
Liu, Y., Guo, H., Zhang, Y., Tang, W., Cheng, X., Li, W., 2018. Heterogeneous activation of peroxymonosulfate by sillenite $Bi_{25}FeO_{40}$: singlet oxygen generation and degradation for aquatic levofloxacin. Chem. Eng. J. 343, 128–137.
Long, Y., Bu, S., Huang, Y., Shao, Y., Xiao, L., Shi, X., 2019. N-doped hierarchically porous carbon for highly efficient metal-free catalytic activation of peroxymonosulfate in water: a non-radical mechanism. Chemosphere 216, 545–555.
Lu, S., Wang, G., Chen, S., Yu, H., Ye, F., Quan, X., 2018. Heterogeneous activation of peroxymonosulfate by $LaFeO_3$ for diclofenac degradation: DFT-assisted mechanistic study and degradation pathways. Chem. Eng. J. 352, 601–611.
Miao, J., Duan, X., Li, J., Dai, J., Liu, B., Wang, S., Zhou, W., Shao, Z., 2019. Boosting performance of lanthanide magnetism perovskite for advanced oxidation through lattice doping with catalytically inert element. Chem. Eng. J. 355, 721–730.
Nie, Y., Zhang, L., Li, Y.Y., Hu, C., 2015. Enhanced Fenton-like degradation of refractory organic compounds by surface complex formation of $LaFeO_3$ and H_2O_2. J. Hazard Mater. 294, 195–200.
Oh, W.D., Dong, Z., Ronn, G., Lim, T.T., 2017. Surface–active bismuth ferrite as superior peroxymonosulfate activator for aqueous sulfamethoxazole removal: performance, mechanism and quantification of sulfate radical. J. Hazard Mater. 325, 71–81.
Pu, J., Nishikado, K., Wang, N., Nguyen, T.T., Maki, T., Qian, E.W., 2018. Core-shell nickel catalysts for the steam reforming of acetic acid. Appl. Catal. B Environ. 224, 69–79.
Qi, C., Liu, X., Ma, J., Lin, C., Li, X., Zhang, H., 2016. Activation of peroxymonosulfate by base: implications for the degradation of organic pollutants. Chemosphere 151, 280–288.
Rabelo-Neto, R.C., Sales, H.B.E., Inocêncio, C.V.M., Varga, E., Oszko, A., Erdohelyi, A., Noronha, F.B., Mattos, L.V., 2018. CO_2 reforming of methane over supported $LaNiO_3$ perovskite-type oxides. Appl. Catal. B Environ. 221, 349–361.
Rao, Y., Han, F., Chen, Q., Wang, D., Xue, D., Wang, H., Pu, S., 2019. Efficient degradation of diclofenac by $LaFeO_3$-catalyzed peroxymonosulfate oxidation—kinetics and toxicity assessment. Chemosphere 218, 299–307.
Rao, Y., Zhang, Y., Han, F., Guo, H., Huang, Y., Li, R., Qi, F., Ma, J., 2018. Heterogeneous activation of peroxymonosulfate by $LaFeO_3$ for diclofenac degradation: DFT-assisted mechanistic study and degradation pathways. Chem. Eng. J. 352, 601–611.
Shao, B., Liu, Z., Zeng, G., Liu, Y., Yang, X., Zhou, C., Chen, M., Liu, Y., Jiang, Y., Yan, M., 2019. Immobilization of laccase on hollow mesoporous carbon nanospheres: noteworthy immobilization, excellent stability and efficacious for antibiotic contaminants removal. J. Hazard Mater. 362, 318–326.
Solís, R.R., Rivas, F.J., Gimeno, O., 2017. Removal of aqueous metazachlor, tembotrione, tritosulfuron and ethofumesate by heterogeneous monopersulfate decomposition on lanthanum-cobalt perovskites. Appl. Catal. B Environ. 200, 83–92.
Soltani, T., Tayyebi, A., Lee, B.K., 2018. Quick and enhanced degradation of bisphenol A by activation of potassium peroxymonosulfate to $SO_4^{\bullet-}$ with Mn-doped $BiFeO_3$ nanoparticles as a heterogeneous Fenton-like catalyst. Appl. Surf. Sci. 441, 853–861.
Su, C., Duan, X., Miao, J., Zhong, Y., Zhou, W., Wang, S., Shao, Z., 2017. Mixed conducting perovskite materials as superior catalysts for fast aqueous-phase advanced oxidation: a mechanistic study. ACS Catal. 7, 388–397.
Wang, G., Cheng, C., Zhu, J., Wang, L., Gao, S., Xia, X., 2019. Enhanced degradation of atrazine by nanoscale $LaFe_{1-x}Cu_xO_{3-\delta}$ perovskite activated peroxymonosulfate: performance and mechanism. Sci. Total Environ. 673, 565–575.
Wang, J., Wang, S., 2018. Activation of persulfate (PS) and peroxymonosulfate (PMS) and application for the degradation of emerging contaminants. Chem. Eng. J. 334, 1502–1517.
Wei, S., He, H., Cheng, Y., Yang, C., Zeng, G., Kang, L., Qian, H., Zhu, C., 2017. Preparation, characterization, and catalytic performances of cobalt catalysts supported on KIT-6 silicas in oxidative desulfurization of dibenzothiophene. Fuel 200, 11–21.
Wu, S., He, H., Inthapanya, X., Yang, C., Lu, L., Zeng, G., Han, Z., 2017a. Role of biochar on composting of organic wastes and remediation of contaminated soils-a review. Environ. Sci. Pollut. Res. 24, 16560–16577.
Wu, S., He, H., Li, X., Yang, C., Zeng, G., Wu, B., He, S., Lu, L., 2018a. Insights into atrazine degradation by persulfate activation using composite of nanoscale zero-valent iron and graphene: performances and mechanisms. Chem. Eng. J. 341, 126–136.
Wu, S., Li, H., Li, X., He, H., Yang, C., 2018b. Performances and mechanisms of efficient degradation of atrazine using peroxymonosulfate and ferrate as oxidants. Chem. Eng. J. 353, 533–541.
Wu, S., Shen, Z., Yang, C., Zhou, Y., Li, X., Zeng, G., Ai, S., He, H., 2017b. Effects of C/N ratio and bulking agent on speciation of Zn and Cu and enzymatic activity during pig manure composting. Int. Biodeterior. Biodegrad. 119, 429–436.
Xiao, P., Zhong, L., Zhu, J., Hong, J., Li, J., Li, H., Zhu, Y., 2015. CO and soot oxidation over macroporous perovskite $LaFeO_3$. Catal. Today 258, 660–667.
Xu, L., Wang, J., 2012. Magnetic nanoscaled Fe_3O_4/CeO_2 composite as an efficient Fenton-like heterogeneous catalyst for degradation of 4-chlorophenol. Environ. Sci. Technol. 46, 10145–10153.
Xu, X., Chen, J., Qu, R., Wang, Z., 2017. Oxidation of Tris (2-chloroethyl) phosphate in aqueous solution by UV-activated peroxymonosulfate: kinetics, water matrix effects, degradation products and reaction pathways. Chemosphere 185, 833–843.
Yang, C., Qian, H., Li, X., Cheng, Y., He, H., Zeng, G., Xi, J., 2018. Simultaneous removal of multicomponent VOCs in biofilters. Trends Biotechnol. 36, 673–685.
Yao, Y., Lian, C., Wu, G., Hu, Y., Wei, F., Yu, M., Wang, S., 2017. Synthesis of "sea urchin"-like carbon nanotubes/porous carbon superstructures derived from waste biomass for treatment of various contaminants. Appl. Catal. B Environ. 219, 563–571.
Yu, J., He, H., Yang, W.L., Yang, C., Zeng, G., Wu, X., 2018. Magnetic bionanoparticles of *Penicillium* sp. yz11-22N2 doped with Fe_3O_4 and encapsulated within PVA-SA gel beads for atrazine removal. Bioresour. Technol. 260, 196–203.
Zang, C., Zhang, X., Hu, S., Chen, F., 2017. The role of exposed facets in the Fenton-like reactivity of CeO_2 nanocrystal to the Orange II. Appl. Catal. B Environ. 216, 106–113.
Zeng, T., Li, S., Hua, J., He, Z., Zhang, X., Feng, H., Song, S., 2018. Synergistically enhancing Fenton-like degradation of organics by *in situ* transformation from Fe_3O_4 microspheres to mesoporous Fe, N-dual doped carbon. Sci. Total Environ. 645, 550–559.
Zhang, C., Wang, C., Gil, S., Boreave, A., Retailleau, L., Guo, Y., Valverde, J.L., Giroir-Fendler, A., 2017. Catalytic oxidation of 1,2-dichloropropane over supported $LaMnO_x$ oxides catalysts. Appl. Catal. B Environ. 201, 552–560.
Zhao, X., Niu, C., Zhang, L., Guo, H., Wen, X., Liang, C., Zeng, G., 2019. Co-Mn layered double hydroxide as an effective heterogeneous catalyst for degradation of organic dyes by activation of peroxymonosulfate. Chemosphere 204, 11–21.
Zheng, Y., Li, K., Wang, H., Tian, D., Wang, Y., Zhu, X., Wei, Y., Zheng, M., Luo, Y., 2017. Designed oxygen carriers from macroporous $LaFeO_3$ supported CeO_2 for chemical-looping reforming of methane. Appl. Catal. B Environ. 202, 51–63.
Zhu, J., Li, H., Zhong, L., Xiao, P., Xu, X., Yang, X., Zhao, Z., Li, J., 2014. Perovskite oxides: preparation, characterizations, and applications in heterogeneous

catalysis. ACS Catal. 4, 2917–2940.
Zhu, C., Yang, W., He, H., Yang, C., Yu, J., Wu, X., Zeng, G., Tarre, S., Green, M., 2018a. Preparation, performance and mechanisms of magnetic Saccharomyces cerevisiae bionanocomposites for atrazine removal. Chemosphere 200, 380–387.
Zhu, C., Zhu, F., Dionysiou, D.D., Zhou, D., Fang, G., Gao, J., 2018b. Contribution of alcohol radicals to contaminant degradation in quenching studies of persulfate activation process. Water Res. 139, 66–73.